

# Active Token Mixer

Guoqiang Wei<sup>1\*</sup> Zhizheng Zhang<sup>2\*</sup> Cuiling Lan<sup>2</sup> Yan Lu<sup>2</sup> Zhibo Chen<sup>1</sup>

<sup>1</sup> University of Science and Technology of China

<sup>2</sup> Microsoft Research Asia

wgq7441@mail.ustc.edu.cn {zhizzhang, culan, yanlu}@microsoft.com chenzhibo@ustc.edu.cn

## Abstract

The three existing dominant network families, i.e., CNNs, Transformers, and MLPs, differ from each other mainly in the ways of fusing spatial contextual information, leaving designing more effective token-mixing mechanisms at the core of backbone architecture development. In this work, we propose an innovative token-mixer, dubbed Active Token Mixer (ATM), to actively incorporate flexible contextual information distributed across different channels from other tokens into the given query token. This fundamental operator actively predicts where to capture useful contexts and learns how to fuse the captured contexts with the query token at channel level. In this way, the spatial range of token-mixing can be expanded to a global scope with limited computational complexity, where the way of token-mixing is reformed. We take ATM as the primary operator and assemble ATMs into a cascade architecture, dubbed **ATMNet**. Extensive experiments demonstrate that ATMNet is generally applicable and comprehensively surpasses different families of SOTA vision backbones by a clear margin on a broad range of vision tasks, including visual recognition and dense prediction tasks. Code is available at <https://github.com/microsoft/ActiveMLP>.

## 1 Introduction

Convolutional neural networks (CNNs) [31, 48, 50, 51, 49, 12, 22, 26, 71, 79] serve as the most prevalent vision backbones for a long time. Inspired by the successes in Natural Language Processing (NLP), DETR [6] and ViT [30] introduce self-attention based model, i.e., Transformer, into computer vision. Afterwards, Transformers spring up and make splendid breakthroughs on various vision tasks [42, 23, 63, 70, 11, 36, 20]. Most recently, the multi-layer perceptrons (MLPs) based architectures [56, 35] have regained their light and been demonstrated capable of achieving stunning results on various vision tasks [57, 56, 8, 35, 77, 54].

Those three categories of architectures differ from each other mainly in their different ways of token mixing. For different architectures, we uniformly refer to each feature vector as one token. CNN-based architectures [48, 22, 26] mix tokens locally within a sliding window of a fixed shape.

Transformer-based architectures [30, 58, 64] perform message passing from tokens in the global scope into the query token based on the pairwise attentions commonly modeled by the affinities between tokens in the embedding space. MLP-based architectures mostly enable spatial information interaction through the fully connected layers across all tokens [56, 57, 24, 54] or certain tokens selected with hand-crafted rules in a deterministic manner [8, 77, 61, 75, 35, 55]. However, the fully connected layer across all tokens makes the model unable to cope with the inputs of variable resolutions. Adopting manually designed rules for token selection relaxes this constraint on fixed resolutions by restricting token mixing within a *deterministic* region, but sacrificing the adaptability to various visual contents of diverse feature patterns.

In this work, we first revisit the token mixing mechanisms in dominant types of architectures from a unified perspective, then propose a novel Active Token Mixer (ATM). As an innovative basic operator, ATM considers two properties of the learned features to actively select the tokens for mixing: 1) the semantics in different spatial positions may correspond to diverse scales and deformations; 2) different semantic attributes of a token would distribute in different channels [3, 68]. As illustrated in Fig. 1 (a), for a query, ATM actively predicts the locations offsets of tokens whose information should be incorporated for interaction. Particularly, ATM predicts the respective offset *channel-wisely* to select the context elements which are then recomposed to a new token. This empowers a more adaptive and flexible information interaction across tokens. We adopt this operation along the horizontal and vertical dimensions in parallel (Fig. 1 (b)), making such predictive context localization easier to be optimized. Then we learn to adaptively fuse the two recomposed tokens and the original query to be the output.

The ATM can serve as a primary operator for constructing backbone architectures. To showcase this, we build a series of model variants with different model scales, named ATMNet-xT/T/S/B/L, respectively. ATMNet shows impressive effectiveness of ATM on a broad range of vision tasks as well as favorable scalability over different model scales. Besides, ATM can also serve as a plug-and-play enhanced replacement of the conventional convolution layers in FPN [37] to enhance the pyramid feature learning for dense prediction tasks (object detection and segmentation).

\*Equal contribution. This work was done when Guoqiang Wei was an intern at MSRA.

Copyright © 2023, Association for the Advancement of Artificial Intelligence (www.aaai.org). All rights reserved.

Our contributions can be summarized below:

- We propose Active Token Mixer (ATM), a basic operator to efficiently enable content-adaptive and flexible global scope token mixing at channel level. It expands the range and reforms the way of message passing.
- We build an efficient vision backbone ATMNet with ATM as its primary ingredient for effective spatial information interaction. For the commonly used neck structure FPN, we build an enhanced FPN, *i.e.*, ATMFPN, powered by ATM, for dense prediction tasks.
- ATMNet achieves strong performance over different model scales and across various vision tasks. For image classification, only trained on ImageNet-1K, ATMNet achieves 82.0% top-1 accuracy with 27M parameters and reaches 84.8% when scaling up to 76M. Moreover, ATMNet outperforms recent prevalent backbones on dense prediction tasks by a significant margin with comparable or even less parameters and computation cost.

## 2 Related Work

### 2.1 CNN based Models

Convolutional neural networks (CNNs) have been the mainstream architectures in computer vision for a long time. The CNN model is originally presented in [32] for document recognition. Beginning with the significant success of AlexNet [31] in ILSVRC 2012, various CNN-based architectures are designed or searched, *e.g.*, Inception [50, 51, 49], VGG [48], ResNet [22], DenseNet [26], ResNeXt [71], EfficientNet [53], MNASNet, [52] and others [62, 18, 43]. In addition, there are a series of works dedicated to improving the convolution layers from different perspectives, *e.g.*, depthwise separable convolution [12, 25, 47] for reduced computation costs and deformable convolution [16, 83] for objects of diverse shapes. It is noteworthy that the deformable convolution also allows learnable token selection for token mixing but ignores the semantic differences across channels [3, 68] and usually suffers from optimization difficulties [7].

### 2.2 Self-attention based Models

[30] firstly introduces a pure self-attention based backbone to computer vision, *i.e.*, ViT, which achieves promising performance on image classification especially trained with extremely large-scale data. [58] improves the training strategy of ViT and proposes a knowledge distillation method, which helps ViT achieve higher performance trained only on ImageNet. Afterwards, various works endeavor to explore efficient vision Transformer architectures, *e.g.*, PVT [64, 65], Swin [42, 41], Twins [13], MViT [73, 34], and others [14, 19, 1, 60, 74, 4, 33]. Transformer also presents its superiority on various tasks, *e.g.*, object detection [6, 84], segmentation [11, 10, 70, 80], pose estimation [36], tracking [63, 9] and GAN [28, 72].

### 2.3 MLP-like Models

Recently, MLP-like models have been reinvigorated. The pioneering works MLP-Mixer [56] and ResMLP [57] stack two types of MLP layers, *i.e.*, token-mixing MLP and

channel-mixing MLP, alternately. The token-mixing MLP enables spatial information interaction over all tokens while the channel-mixing MLP mixes information across all channels within each token. ViP [24] and sMLP [54] encode the feature representations along two axial dimensions to improve MLPs' efficiency and capability. Shift [61], ASMLP [35] and S<sup>2</sup>MLP [75] perform spatial information mixing with spatial shift operations along different dimensions. CycleMLP [8], WaveMLP [55] and MorphMLP [77] restrict the spatial information interaction within *hand-craft fixed local* windows in a *deterministic* way. As opposed to them, our ATM achieves a *learnable content-adaptive token-mixing*, which considers the diverse semantics attributed in different channels and spatial positions with global receptive fields, so that it can attain high flexibility and strong modeling capacity.

## 3 Method

### 3.1 A Unified Perspective of Token Mixing

For most prevailing model architectures, the input image is first patchified into a feature tensor  $\mathbf{X} \in \mathbb{R}^{H \times W \times C}$  with the height  $H$ , the width  $W$  and the number of channels  $C$ . In vision tasks, token mixing is especially critical since the contextual information is inevitably required for understanding visual semantics. Before introducing our proposed method, we firstly review different token mixing mechanisms in the literature from a unified perspective. Mathematically, we formulate token mixing with a unified function:

$$f(\mathbf{X})|_{\mathbf{x}^q} = \sum_{k \in \mathcal{N}(\mathbf{x}^q)} \omega^{k \rightarrow q} * g(\mathbf{x}^k), \quad (1)$$

where  $\mathbf{x}^q$  denotes the query token while  $\mathcal{N}(\mathbf{x}^q)$  refers to a set of its contextual tokens.  $\omega^{k \rightarrow q}$  is the weight determining the degree of message passing from  $\mathbf{x}^k$  to  $\mathbf{x}^q$ .  $g(\cdot)$  is an embedding function.  $*$  is a unified representation for element-wise or matrix multiplication.

For conventional CNNs,  $g(\cdot)$  is an identity function, and  $\omega^{k \rightarrow q} \in \mathbb{R}^{C \times C}$  corresponds to the convolutional kernels shared for different queries, and the message passing is restricted within a fixed-size sliding window  $\mathcal{N}(\cdot)$ . Transformers achieve a non-local  $\mathcal{N}(\cdot)$  and adopt a computationally expensive  $\omega^{k \rightarrow q} \in \mathbb{R}^C$  through calculating the affinity between  $\mathbf{x}^k$  and  $\mathbf{x}^q$  in the embedding space. In recent MLP-like backbones [8, 57, 56, 77, 35, 54, 55],  $\mathcal{N}(\cdot)$  and  $\omega^{k \rightarrow q}$  are manually designed to perform token mixing in a *deterministic* way, leading to the *lack of content adaptivity*. In Transformers or MLPs,  $g(\cdot)$  is commonly a learnable embedding function.

### 3.2 Active Token Mixer

Based on the token mixing methods detailed in Sec. 3.1, we have two key observations: 1) For the spatial dimension, visual objects/stuffs present diverse shapes and deformations. Therefore, information mixing within a fixed-range  $\mathcal{N}(\cdot)$  [57, 8, 56, 35] is inefficient and inadequate. The adaptive  $\omega^{k \rightarrow q}$  and  $\mathcal{N}(\cdot)$  for message passing are desirable for extracting visual representations. 2) For the channel dimension, multiple semantic attributes carried in one token would

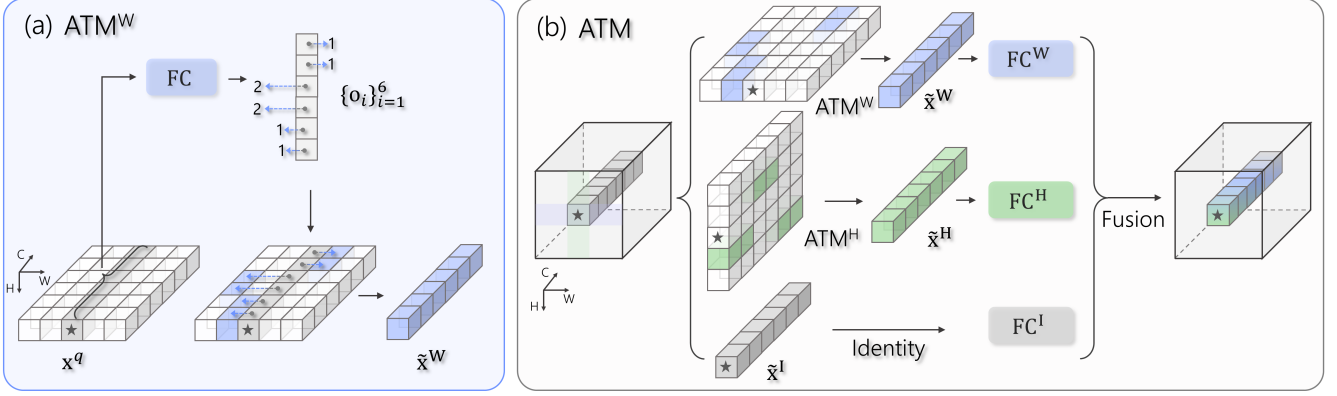


Figure 1: Illustration of our proposed Active Token Mixer (ATM). (a) ATM along the horizontal (width) dimension. For a query  $\mathbf{x}^q$ , ATM actively captures the useful contexts by recomposing the elements from selected tokens into  $\tilde{\mathbf{x}}^W \in \mathbb{R}^C$  based on the learned channel-wise offsets. (b) ATM module consisting of  $\text{ATM}^W$  along horizontal dimension,  $\text{ATM}^H$  along vertical dimension, and the identity branch  $\text{ATM}^I$ . The two recomposed tokens ( $\tilde{\mathbf{x}}^W, \tilde{\mathbf{x}}^H$ ) and the original  $\tilde{\mathbf{x}}^I$  are then adaptively fused after being embedded by  $FC^{\{W,H,I\}}$ .

distribute in its different channels [3, 68]. The token-level message passing with  $\omega^{k \rightarrow q} \in \mathbb{R}$  shared over all channels can not treat different semantics adaptively and limits their full use, thus is less effective [57, 56]. In this work, *we pinpoint the importance of more fine-grained message passing for treating different semantics adaptively.*

To address the aforementioned limitations in existing token-mixing methods, we propose Active Token Mixer (ATM) as shown in Fig. 1. It first predicts the relative locations of useful contextual tokens along each direction at channel level, then learns to fuse the contextual tokens and query token. These two steps correspond to learn **where** the useful context tokens locate in and **how** to fuse them with the original information, respectively.

Drawing on the success of multi-branch design in [24, 8, 35], we propose a three-branch architecture for facilitating the context localization along different directions. Two branches are responsible for recomposing tokens into a new one along two axial directions separately as shown in Fig. 1 (b). In addition, we adopt an identity branch to preserve the original query information. The two recomposed tokens and query are further mixed as the final output.

**ATM along the horizontal dimension** We illustrate the ATM along the horizontal (width) dimension, denoted by  $\text{ATM}^W$ , in Fig. 1 (a). Given the query  $\mathbf{x}^q \in \mathbb{R}^C$  (marked with  $\star$ ), we first feed it into a FC layer to adaptively predict  $C$  offsets  $\mathcal{O} = \{o_i\}_{i=1}^C$  for context localization. Note that we impose no constraint on the offset generation, thus  $\mathcal{N}(\mathbf{x}^q)$  is allowed to be extended to all spatial positions along the horizontal direction. In this way, ATM can incorporate the information from the global scope, wherever needed, into  $\mathbf{x}^q$  in a flexible and active manner. The predicted offsets determine the tokens in  $\mathcal{N}(\cdot)$  per channel, which are used to recombine the selected tokens into a new token  $\tilde{\mathbf{x}}^W \in \mathbb{R}^C$  as output of  $\text{ATM}^W$ :

$$\tilde{\mathbf{x}}^W = [\mathbf{X}_{[i,j+o_1,1]}, \mathbf{X}_{[i,j+o_2,2]}, \dots, \mathbf{X}_{[i,j+o_C,C]}]^T, \quad (2)$$

where  $\mathbf{X}_{[i,j+o,c]}$  denotes the  $c^{\text{th}}$  channel element of the token at spatial position  $[i, j + o]$  where  $[i, j]$  is the position of  $\mathbf{x}^q$ .  $\text{ATM}^W$  is capable of mixing information horizontally and globally into  $\tilde{\mathbf{x}}^W$ .

**ATM along the vertical dimension** Likewise, another  $\text{ATM}^H$  branch is adopted to recompose a token  $\tilde{\mathbf{x}}^H$  along the vertical (height) dimension.

**Fusion** Here, we introduce how to fuse the recomposed  $\tilde{\mathbf{x}}^W, \tilde{\mathbf{x}}^H$  and the original  $\tilde{\mathbf{x}}^I$  into the final token-mixing result. First, we adopt three FC layers  $FC^{\{W,H,I\}}$  to embed  $\tilde{\mathbf{x}}^{\{W,H,I\}}$  to  $\hat{\mathbf{x}}^{\{W,H,I\}}$ , respectively, which are then mixed with learned weights, formulated as:

$$\hat{\mathbf{x}} = \alpha^W \odot \tilde{\mathbf{x}}^W + \alpha^H \odot \tilde{\mathbf{x}}^H + \alpha^I \odot \tilde{\mathbf{x}}^I, \quad (3)$$

where  $\odot$  denotes element-wise multiplication.  $\alpha^{\{W,H,I\}} \in \mathbb{R}^C$  are learned from the summation  $\hat{\mathbf{x}}^\Sigma$  of  $\hat{\mathbf{x}}^{\{W,H,I\}}$  with  $W^{\{W,H,I\}} \in \mathbb{R}^{C \times C}$ :

$$[\alpha^W, \alpha^H, \alpha^I] = \sigma([W^W \cdot \hat{\mathbf{x}}^\Sigma, W^H \cdot \hat{\mathbf{x}}^\Sigma, W^I \cdot \hat{\mathbf{x}}^\Sigma]), \quad (4)$$

where  $\sigma(\cdot)$  is a *softmax* function for normalizing each channel separately.

**Discussion** Our ATM has three hallmarks: 1) *Content adaptivity*. The context selection/localization is adaptively learned for the query token in an active way, instead of being passively determined by manual designed rules [8, 35, 75, 77]. 2) *Flexibility*. In general, different channels are characterized with different semantics. Our proposed ATM enables to dynamically select context tokens at the channel level from a global range  $\mathcal{N}(\cdot)$ , adaptive to visual contents with various scales and deformations. 3) *Efficiency*. By incorporating contexts from  $C$  tokens into the two recomposed tokens, the computation complexity of ATM is  $\mathcal{O}(HWC^2)$ , which is linear with the input resolution and is agnostic to the receptive fields, making it computation-friendly to larger-size images used in object detection and segmentation tasks.

Model	Size	#P.(M)	FLOPs(G)	Top-1(%)
ResNet18 [22]	224 <sup>2</sup>	12	1.8	69.8
ResMLP-S12 [57]	224 <sup>2</sup>	15	3.0	76.6
CycleMLP-B1 [8]	224 <sup>2</sup>	15	2.1	78.9
ATMNet-xT	224 <sup>2</sup>	15	2.2	<b>79.7</b>
ResNet50 [22, 67]	224 <sup>2</sup>	26	4.1	79.8
DeiT-S [58]	224 <sup>2</sup>	22	4.6	79.8
DeiT III-S [59]	224 <sup>2</sup>	22	4.6	81.4
PVT-S [64]	224 <sup>2</sup>	25	3.8	79.8
Swin-T [42]	224 <sup>2</sup>	29	4.6	81.2
TwinsP-S [13]	224 <sup>2</sup>	24	3.8	81.2
Twins-S [13]	224 <sup>2</sup>	24	2.9	81.7
ResMLP-S24 [57]	224 <sup>2</sup>	30	6.0	79.4
ASMLP-T [35]	224 <sup>2</sup>	28	4.4	81.3
ViP-S [24]	224 <sup>2</sup>	25	6.9	81.5
MorphMLP-T [77]	224 <sup>2</sup>	23	3.9	81.6
CycleMLP-B2 [8]	224 <sup>2</sup>	27	3.9	81.6
Shift-T [61]	224 <sup>2</sup>	29	4.5	81.7
sMLP-T [54]	224 <sup>2</sup>	24	5.0	81.9
ATMNet-T	224 <sup>2</sup>	27	4.0	<b>82.0</b>
PVT-M [64]	224 <sup>2</sup>	44	6.7	81.2
TwinsP-B [13]	224 <sup>2</sup>	44	6.7	82.7
MorphMLP-S [77]	224 <sup>2</sup>	38	7.0	82.6
CycleMLP-B3 [8]	224 <sup>2</sup>	38	6.9	82.6
DeiT III-M [59]	224 <sup>2</sup>	39	8.0	83.0
ATMNet-S	224 <sup>2</sup>	39	6.9	<b>83.1</b>

Model	Size	#P.(M)	FLOPs(G)	Top-1(%)
PVT-L [64]	224 <sup>2</sup>	61	9.8	81.7
Swin-S [42]	224 <sup>2</sup>	50	8.7	83.2
Twins-B [13]	224 <sup>2</sup>	56	8.6	83.2
Mixer-B/16 [56]	224 <sup>2</sup>	59	12.7	76.4
ViP-M [24]	224 <sup>2</sup>	55	16.3	82.7
Shift-S [61]	224 <sup>2</sup>	50	8.8	82.8
CycleMLP-B4 [8]	224 <sup>2</sup>	52	10.1	83.0
ASMLP-S [35]	224 <sup>2</sup>	50	8.5	83.1
MorphMLP-B [77]	224 <sup>2</sup>	58	10.2	83.2
ATMNet-B	224 <sup>2</sup>	52	10.1	<b>83.5</b>
DeiT-B [58]	224 <sup>2</sup>	86	17.5	81.8
DeiT III-B [59]	224 <sup>2</sup>	87	17.5	<b>83.8</b>
Swin-B [42]	224 <sup>2</sup>	88	15.4	83.5
S <sup>2</sup> MLP-W [75]	224 <sup>2</sup>	71	14.0	80.0
CycleMLP-B5 [8]	224 <sup>2</sup>	76	15.3	83.1
ViP-L [24]	224 <sup>2</sup>	88	24.4	83.2
Shift-B [61]	224 <sup>2</sup>	89	15.6	83.3
ASMLP-B [35]	224 <sup>2</sup>	88	15.2	83.3
MorphMLP-L [77]	224 <sup>2</sup>	76	12.5	83.4
sMLP-B [54]	224 <sup>2</sup>	66	14.0	83.4
ATMNet-L	224 <sup>2</sup>	76	12.3	<b>83.8</b>
ViT-B/16 <sup>†</sup> [30]	384 <sup>2</sup>	86	55.4	77.9
DeiT-B <sup>†</sup> [58]	384 <sup>2</sup>	86	55.4	83.1
Swin-B <sup>†</sup> [42]	384 <sup>2</sup>	88	47.1	84.5
ATMNet-L <sup>†</sup>	384 <sup>2</sup>	76	36.4	<b>84.8</b>

Table 1: Comparisons with state-of-the-art models on ImageNet-1K without extra data. All models are trained with input size of 224×224, except <sup>†</sup> with 384×384.

Compared with the conventional convolutions, ATM is able to enlarge its receptive field to global-scope flexibly with constant computation cost. Compared with the multi-head self-attention in Transformers, ATM globally mixes token information per channel with the actively learned offsets, avoiding the computation-consuming attention calculation. ATM may be reminiscent of the deformable convolution [16, 83]. In fact, there are two crucial differences: 1) The learned offsets in deformable convolutions are shared over all channels, without consideration on semantic differences across channels. Our ATM can incorporate contextual information in channel wise, achieving a more flexible and fine-grained context exploitation mechanism in token mixing. 2) We decouple the learning of context localization along different directions, making ATMNet easier to be optimized.

### 3.3 Model Architectures

**ATM Block** We build our ATMNet by stacking multiple ATM blocks in sequence. Here, we introduce the architecture of an ATM block. For the output  $\mathbf{X}^{l-1}$  of the  $(l-1)$ -th block  $\text{ATM}^{l-1}$ , we feed it to the  $l$ -th block  $\text{ATM}^l$  for token mixing. Further, we use an MLP module to further modulate the feature along its channel dimension. Skip connections are adopted to facilitate the training. The entire process can

be formulated as:

$$\hat{\mathbf{X}}^l = \text{ATM}^l(\text{LN}(\mathbf{X}^{l-1})) + \mathbf{X}^{l-1}, \quad (5)$$

$$\mathbf{X}^l = \text{MLP}^l(\text{LN}(\hat{\mathbf{X}}^l)) + \hat{\mathbf{X}}^l, \quad (6)$$

where  $\text{LN}$  is LayerNorm [2].

**ATMNet** Following the typical hierarchical architecture designs [22, 42], we provide five four-stage backbone architecture variants with different channel dimensions and numbers of the ATM blocks, which are ATMNet-xT/T/S/B/L, respectively. Note that the offset generation layer is shared across the tokens within each ATM branch. Here, the awareness of the position of query token can facilitate offsets prediction. We thus introduce one positional encoding generator (PEG) [14] for each stage before ATM, which helps a little for dense prediction tasks. More details are placed in the supplementary.

**ATMFpn** In addition to the strong capability of constructing vision backbones, ATM is also an enhanced alternative for conventional convolutions in convolution-based decoders for downstream tasks. We replace the convolutions in the prevailing FPN [38], which is widely applied as the neck for object detection and segmentation, with our ATM and name this new neck as **ATMFpn**. We demonstrate the effectiveness of our ATMFpn in Table 7.



Backbone	#P.(M)	FLOPs(G)	mIoU(ss)
CycleMLP-B1 [8]	18.9	32.8	40.8
WaveMLP-T [55]	19.3	-	41.2
ATMNet-xT	19.1	33.1	<b>43.0</b>
Swin-T [42]	31.9	46	41.5
Twins-S [13]	28.3	37	43.2
MorphMLP-T [77]	26.4	-	43.0
CycleMLP-B2 [8]	30.6	42.0	43.4
Wave-MLP-S [55]	31.2	-	44.4
ATMNet-T	30.9	42.4	<b>45.8</b>
Swin-S [42]	53.2	70	45.2
Twins-B [13]	60.4	67	45.3
CycleMLP-B3 [8]	42.1	57.5	44.3
WaveMLP-M [55]	43.3	-	46.8
ATMNet-S	42.4	57.8	<b>47.3</b>
Swin-B [42]	91.2	107	46.0
Twins-L [13]	103.7	102	46.7
MorphMLP-B [77]	59.3	-	45.9
CycleMLP-B5 [8]	79.4	86.0	45.5
ATMNet-B	55.9	74.7	47.7
ATMNet-L	79.8	86.6	<b>48.1</b>

Table 2: Semantic segmentation results on ADE20K val with Semantic FPN [29]. FLOPs are evaluated on 512×512 resolution. All backbones are pretrained on ImageNet-1K.

## 4 Experiments

### 4.1 ImageNet-1K Classification

**Settings** We train our models on the ImageNet-1K dataset [17] from scratch, which contains 1.2M training images and 50K validation images evenly spreading 1,000 categories. We report the top-1 accuracy on the validation set following the standard practice in this community [42, 43, 64, 8]. Our implementation is established with PyTorch [45] and base on the timm [66] repository. For fair comparisons, our training strategy is mostly inherited from DeiT [58], which includes RandAugment [15], Mixup [78], Cutmix [76], Random erasing [81] and stochastic depth [27]. The optimizer is AdamW [44] with the momentum of 0.9 and weight decay of  $5 \times 10^{-2}$  by default. All models are trained with input size of 224×224 for 300 epochs with 5-epoch warm-up and batch size of 1024. For 384×384 resolution, we finetune the models for 30 epochs with the learning rate of  $5e - 6$ . More details are shown in Table 9.

**Results** We report the top-1 accuracy comparison between our ATMNet with recent CNN-, Transformer- and MLP-based backbones in Table 1, where all methods are categorized into different groups w.r.t. the model size (#Parameters) and computation complexity (FLOPs). All our different variants achieve higher accuracy compared with the scale-comparable methods. 1) Our ATMNet-T, -B, and -L variants outperform the prominent Transformer Swin-T, -S, and -B by +0.8%, +0.3% and +0.3% with comparable parameters and FLOPs. For larger models, ATMNet-L↑ surpasses Swin-B↑ with -23% computation cost. 2) Our ATMNet also surpasses all recent MLP-like backbones (ASMLP, CycleMLP,

Backbone	#P.(M)	FLOPs(G)	mIoU(ss)	mIoU(ms)
ATMNet-xT	45	889	44.3	45.4
Swin-T [42]	60	945	44.5	45.8
Twins-S [13]	54	931	46.2	47.1
ConvNeXt-T [43]	60	939	-	46.7
ASMLP-T [35]	60	937	-	46.5
CycleMLP-T [8]	60	937	-	47.1
ATMNet-T	57	927	<b>46.5</b>	<b>47.6</b>
Swin-S [42]	81	1038	47.6	49.5
Twins-B [13]	89	1078	47.7	48.9
ConvNeXt-S [43]	82	1027	-	49.6
ASMLP-S [35]	81	1024	-	49.2
CycleMLP-S [8]	81	1024	-	49.6
ATMNet-B	82	1055	<b>48.7</b>	<b>49.8</b>
Swin-B [42]	121	1188	48.1	49.7
Twins-L [13]	133	1236	48.8	50.2
ConvNeXt-B [43]	122	1170	-	49.9
ASMLP-B [35]	121	1166	-	49.5
CycleMLP-B [8]	121	1166	-	49.7
ATMNet-S	69	988	48.4	49.5
ATMNet-L	108	1106	<b>50.1</b>	<b>51.1</b>

Table 3: Semantic segmentation results on ADE20K val with UperNet [69]. FLOPs are evaluated on 512×2048 resolution. All backbones are pretrained on ImageNet-1K.

ViP, and etc). Compared with the recent CycleMLP mixing tokens in a *deterministic and local* manner, our five variants outperforms the corresponding CycleMLP variants by +0.8%, 0.5%, +0.4%, +0.5% and +0.7% respectively, with comparable computation cost.

Note that some MLP-like backbones (*e.g.*, MLP-Mixer, ResMLP, gMLP, ResMLP, ViP, sMLP and etc) in Table 1 are not validated in downstream dense prediction tasks, where the most architectures are not compatible with various input resolutions. In contrast, our ATMNet is capable of dealing with different input scales, and shows pronounced performance on dense prediction tasks, which will be shown in the following sections.

### 4.2 Semantic Segmentation

**Settings** The semantic segmentation is validated on the ADE20K [82], which contains 20K training and 2K validation images. To compare with more existing backbone designs, we adopt the ATMNet models initialized with the pre-trained weights on ImageNet-1K as the backbones for two widely used frameworks, Semantic FPN [29] and UperNet [69].

For the experiments on Semantic FPN framework, we mainly follow the setting of PVT [64] to train models for 40K iterations with the batchsize of 32 (8 GPUs with 4 images per GPU). We use AdamW [44] optimizer with the initial learning rate of  $2e^{-4}$  and the weight decay of 0.01. The image is randomly resized and cropped to 512×512 for training. We set the stochastic depths as 0.1, 0.1, 0.2, 0.2 and 0.2 for ATMNet-xT, -T, -S, -B and -L respectively.

For the experiments on UperNet framework, we mainly follow the setting of Swin [42] to train models for 160K

Backbone	#Params. FLOPs		RetinaNet 1×						RetinaNet 3× MS					
	(M)	(G)	$AP^b$	$AP_{50}^b$	$AP_{75}^b$	$AP_S$	$AP_M$	$AP_L$	$AP^b$	$AP_{50}^b$	$AP_{75}^b$	$AP_S$	$AP_M$	$AP_L$
Swin-T [42]	39	245	41.5	62.1	44.2	25.1	44.9	55.5	45.0	65.9	48.4	29.7	48.9	58.1
Twins-S [13]	34	286	43.0	64.1	46.0	<b>27.5</b>	46.3	57.3	45.2	66.5	48.6	30.0	48.8	58.9
CycleMLP-B2 [8]	37	231	40.9	61.8	43.4	23.4	44.7	53.4	-	-	-	-	-	-
WaveMLP-S [55]	37	231	43.4	64.4	46.5	26.6	47.1	57.1	-	-	-	-	-	-
ATMNet-xT	25	196	41.2	62.3	43.7	24.4	45.3	54.2	43.7	64.7	46.7	28.9	47.4	57.4
ATMNet-T	37	233	<b>43.6</b>	<b>64.9</b>	<b>46.8</b>	27.2	<b>47.5</b>	<b>57.9</b>	<b>45.8</b>	<b>66.9</b>	<b>49.2</b>	<b>29.9</b>	<b>49.3</b>	<b>59.9</b>
Twins-L [13]	111	528	45.7	67.1	49.2	-	-	-	-	-	-	-	-	-
Swin-B [42]	98	477	44.7	65.9	47.8	-	-	-	45.8	66.4	49.1	29.9	49.4	60.3
CycleMLP-B5 [8]	86	402	42.7	63.3	45.3	24.1	46.3	57.4	-	-	-	-	-	-
WaveMLP-B [55]	66	334	44.2	65.1	47.1	27.1	47.8	58.9	-	-	-	-	-	-
ATMNet-S	48	293	45.4	66.7	48.5	28.3	49.7	59.7	46.3	68.0	49.5	30.4	50.6	59.9
ATMNet-B	62	359	45.6	67.2	48.9	28.9	49.6	60.5	47.7	69.2	50.9	<b>33.1</b>	51.6	61.8
ATMNet-L	86	405	<b>46.1</b>	<b>67.4</b>	<b>49.4</b>	<b>29.9</b>	<b>50.1</b>	<b>61.0</b>	<b>48.1</b>	<b>69.5</b>	<b>51.8</b>	31.7	<b>52.1</b>	<b>63.0</b>

Table 4: Object detection results on COCO val2017 with RetinaNet [39] 1× and 3× MS. FLOPs are evaluated with resolution 800×1280.

Backbone	#Params. FLOPs		Mask R-CNN 1×						Mask R-CNN 3× MS					
	(M)	(G)	$AP^b$	$AP_{50}^b$	$AP_{75}^b$	$AP^m$	$AP_{50}^m$	$AP_{75}^m$	$AP^b$	$AP_{50}^b$	$AP_{75}^b$	$AP^m$	$AP_{50}^m$	$AP_{75}^m$
Swin-T [42]	48	264	42.2	64.6	46.2	39.1	61.6	42.0	46.0	68.2	50.2	41.6	65.1	44.8
ConvNeXt-T [43]	48	262	-	-	-	-	-	-	46.2	67.9	50.8	41.7	65.0	44.9
Twins-S [13]	44	228	43.4	66.0	47.3	40.3	63.2	43.4	46.8	<b>69.2</b>	51.2	42.6	66.3	45.8
ASMLP-T [35]	48	260	-	-	-	-	-	-	46.0	67.5	50.7	41.5	64.6	44.5
CycleMLP-B2 [8]	47	250	42.1	64.0	45.7	38.9	61.2	41.8	-	-	-	-	-	-
WaveMLP-S [55]	47	250	44.0	65.8	48.2	40.0	63.1	42.9	-	-	-	-	-	-
ATMNet-xT	35	215	42.8	64.9	46.9	39.5	62.1	42.5	45.0	67.4	49.5	41.1	64.4	44.2
ATMNet-T	47	251	<b>44.8</b>	<b>66.9</b>	<b>49.0</b>	<b>41.0</b>	<b>64.2</b>	<b>44.3</b>	<b>47.1</b>	69.0	<b>51.7</b>	<b>42.7</b>	<b>66.5</b>	<b>46.0</b>
Twins-L [13]	120	474	45.9	-	-	41.6	-	-	-	-	-	-	-	-
Swin-B [42]	107	496	45.5	-	-	41.3	-	-	48.5	69.8	53.2	43.4	66.8	46.9
MViT-B [73]	73	438	-	-	-	-	-	-	48.8	71.2	53.5	44.2	68.4	47.6
CycleMLP-B5 [8]	95	421	44.1	65.5	48.4	40.1	62.8	43.0	-	-	-	-	-	-
WaveMLP-B [55]	75	353	45.7	67.5	50.1	27.8	49.2	59.7	-	-	-	-	-	-
ATMNet-S	58	311	46.0	68.2	50.4	42.0	65.3	45.5	48.1	69.7	52.9	43.4	67.2	46.7
ATMNet-B	72	377	46.5	68.6	51.0	42.5	66.1	45.8	49.0	70.7	54.0	43.9	67.7	47.5
ATMNet-L	96	424	<b>47.4</b>	<b>69.9</b>	<b>52.0</b>	<b>43.2</b>	<b>67.3</b>	<b>46.5</b>	<b>49.5</b>	<b>71.5</b>	<b>54.3</b>	<b>44.5</b>	<b>68.7</b>	<b>48.1</b>

Table 5: Object detection results on COCO val2017 with Mask R-CNN [21] 1× and 3× MS. FLOPs are evaluated with resolution 800×1280.

steps with the batchsize of 16 (8 GPUs with 2 images per GPU). We adopt the AdamW [44] optimizer with the initial learning rate of  $6e^{-5}$  and the weight decay of 0.01. All models are trained with the input size of 512×512. We set the stochastic depths as 0.1, 0.1, 0.2, 0.2 and 0.2 for ATMNet-xT, -T, -S, -B and -L respectively. We adopt mIoU and Multi-Scale ([0.5, 0.75, 1.0, 1.25, 1.5, 1.75]) mIoU as the evaluation metrics.

**Results** The results on top of UperNet and Semantic FPN are shown in Table 2 and Table 3. For different model scales, ATMNet outperforms all previous methods with comparable computation costs. The largest ATMNet-L with Semantic FPN outperforms previous state-of-the-art Twins-L by **+1.4** mIoU with **-23%** parameters and **-16%** FLOPs. ATMNet-L also achieves the new state-of-the-art (**51.1** ms mIoU) with

UperNet, which surpasses the representative network Swin-B by **+1.4** mIoU with **-10%** parameters. Note that ATMNet-S achieves comparable performance with Swin-B, but only requires about **-50%** parameters.

It also shows that most previous MLP-like backbones (e.g., CycleMLP, ASMLP, MorphMLP) perform better than Transformer-based Swin/Twins for smaller models, but lag behind them for larger models. These *manually designed* token mixing methods within them leads to remarkable limitations in exploring rich feature patterns, while the global-scope attention in Transformers allows extracting better features as model scaling up. In contrast, ATMNet shows its strong capability and scalability on segmentation over different model scales, especially for the large-scale models. The superiority of ATMNet lies in the flexibility of ATM, which provides great capability to exploit sufficient features

Backbone	#Params. FLOPs		Cascade Mask R-CNN 1×						Cascade Mask R-CNN 3× MS					
	(M)	(G)	AP <sup>b</sup>	AP <sup>b</sup> <sub>50</sub>	AP <sup>b</sup> <sub>75</sub>	AP <sup>m</sup>	AP <sup>m</sup> <sub>50</sub>	AP <sup>m</sup> <sub>75</sub>	AP <sup>b</sup>	AP <sup>b</sup> <sub>50</sub>	AP <sup>b</sup> <sub>75</sub>	AP <sup>m</sup>	AP <sup>m</sup> <sub>50</sub>	AP <sup>m</sup> <sub>75</sub>
Deit-S [58]	80	889	-	-	-	-	-	-	48.0	67.2	51.7	41.4	64.2	44.3
Swin-T [42]	86	745	48.1	67.1	52.2	41.7	64.4	45.0	50.4	69.2	54.7	43.7	66.6	47.3
ConvNeXt-T [43]	86	741	-	-	-	-	-	-	50.4	69.1	54.8	43.7	66.5	47.3
AS-MLP-T [35]	86	739	-	-	-	-	-	-	50.1	68.8	54.3	43.5	66.3	46.9
Shift-T [61]	86	743	-	-	-	-	-	-	50.3	68.6	54.7	43.4	66.2	47.0
ATMNet-xT	73	693	47.6	66.5	51.4	41.3	63.6	44.6	50.0	68.7	54.4	43.5	66.2	46.8
ATMNet-T	85	730	<b>49.4</b>	<b>68.3</b>	<b>53.4</b>	<b>42.8</b>	<b>65.7</b>	<b>45.9</b>	<b>51.3</b>	<b>70.4</b>	<b>55.6</b>	<b>44.6</b>	<b>67.7</b>	<b>48.4</b>
Swin-B [42]	145	982	50.8	70.1	55.1	43.9	67.4	47.4	51.9	70.5	56.4	45.0	68.1	48.9
ConvNeXt-B [43]	146	964	-	-	-	-	-	-	52.7	71.3	57.2	45.6	68.9	49.5
ASMLP-B [35]	145	961	-	-	-	-	-	-	51.5	69.8	55.8	44.6	67.6	48.2
ATMNet-S	96	790	51.0	70.3	55.4	44.2	67.5	47.6	51.5	70.3	55.9	44.8	68.0	48.6
ATMNet-B	110	856	51.3	70.4	55.7	44.6	68.0	48.2	52.5	71.6	57.0	45.6	69.1	49.5
ATMNet-L	134	902	<b>51.8</b>	<b>70.9</b>	<b>56.3</b>	<b>44.8</b>	<b>68.4</b>	<b>48.4</b>	<b>53.3</b>	<b>72.1</b>	<b>57.9</b>	<b>46.3</b>	<b>69.8</b>	<b>50.4</b>

Table 6: Object detection results on COCO val2017 with Cascade Mask R-CNN [5] 1× and 3× MS. FLOPs are evaluated with resolution 800×1280.

from visual signals with various scales and deformations, especially for the pixel-level tasks heavily relying on spatial information interaction.

### 4.3 Object Detection

**Settings** The object detection is evaluated on the COCO [40] dataset, which contains 118K and 5K images for the training and validation. For thorough comparison, we adopt our ImageNet-1K pretrained ATMNet as the backbone on top of three representative detection frameworks, *i.e.*, Mask R-CNN [21], RetinaNet [39] and Cascade Mask R-CNN [5, 21].

Following the common practices in this field [42, 19, 8, 64, 55], we report the standard 1× (MS) schedule and 3× MS schedule detection results on COCO 2017 val for different frameworks. For 1× schedule, we train the model with the single-scale inputs for 12 epochs with the learning rate decayed at 8 and 11 epochs. The image is resized to the shorter side of 800 pixels, while the longer side does not exceed 1333 pixels. For 3× schedule, we train the model for 36 epochs with the learning rate decayed at 27 and 33 epochs. For MS training, the image is resized to the shorter side between 480 and 800 while the longer side no longer than 1333. All models are trained using AdamW [44] optimizer with the batch size of 16 (8 GPUs with 2 images per GPU). Stochastic depths are set as 0.1, 0.1, 0.3, 0.5 and 0.6 for ATMNet-xT, -T, -S, -B and -L, respectively, to avoid overfitting.

**Results** The object detection results for Mask R-CNN 1× and 3× (MS) are shown in Table 5. Thanks to ATM’s flexibility and effectiveness for token mixing, our ATMNet obtains promising results on the challenging object detection. ATMNet achieves the state-of-the-art for the most model scales with different detectors. For the Mask R-CNN 1× setting, our different model variants outperform the corresponding parameter-comparable Swin variants by **+2.6/+1.9** and **+1.9/+1.9** mAP<sup>b</sup>/mAP<sup>m</sup> respectively, which demonstrates

the ATMNet’s superiority on dense prediction task, where the input is usually with larger resolution. For the largest models, ATMNet-L surpasses the state-of-the-art Twins-L by **+1.5** mAP<sup>b</sup> with **-20%** parameters. The comparisons with RetinaNet 1×/3× and Cascade Mask R-CNN 1×/3× can be found in Table 4 and Table 6.

Backbone	Neck	Semantic FPN		Mask R-CNN	
		FLOPs	mIoU	FLOPs	AP <sup>b</sup>
ResNet-50	FPN	45.9	37.3	259.8	38.0
	ATMFpn	48.9	40.3 <sup>↑3.0</sup>	298.9	39.9 <sup>↑1.9</sup>
Swin-Tiny	FPN	47.5	41.5	267.0	42.2
	ATMFpn	47.5	43.7 <sup>↑2.2</sup>	267.1	43.5 <sup>↑1.3</sup>
ATMNet-T	FPN	42.4	45.8	251.1	44.8
	ATMFpn	41.4	46.5 <sup>↑0.7</sup>	247.0	45.6 <sup>↑0.8</sup>
ATMNet-L	FPN	86.6	48.1	423.7	47.4
	ATMFpn	86.6	48.3 <sup>↑0.2</sup>	423.8	48.4 <sup>↑1.0</sup>

Table 7: FPN/ATMFpn for semantic segmentation with Semantic FPN and object detection with Mask R-CNN 1×.

### 4.4 ATMFpn

Our proposed ATM can be adopted not only for constructing vision backbones, but also as an enhanced alternative for convolution-based decoders. Based on FPN [38], we build an ATMFpn neck with ATM, and report the results on different backbones for object detection and semantic segmentation in Table 7. With comparable computation cost, ResNet-50 with ATMFpn outperforms the naive FPN by **+3.0** mIoU/**+1.9** AP<sup>b</sup> for segmentation and object detection respectively. ATMFpn also helps improve the performance for the backbone of Swin and ATMNet. Thanks to the flexibility, our proposed ATM is basically applicable for extracting better visual feature representations.

ID	Model	FLOPs	INT	COCO	ADE20K
①	Baseline	3.890	79.3	36.0	37.9
②	ATMNet w/o PEG	3.924	82.0 $\uparrow$ 2.7	43.4 $\uparrow$ 7.4	45.6 $\uparrow$ 7.7
③	ATMNet	3.972	82.0 $\uparrow$ 2.7	43.6 $\uparrow$ 7.6	45.8 $\uparrow$ 7.9

Table 8: Ablation study. FLOPs are obtained on ImageNet-1K with input resolution of  $224 \times 224$ . COCO: AP<sup>b</sup> for RetinaNet 1 $\times$ . ADE20K: mIoU for Semantic FPN.

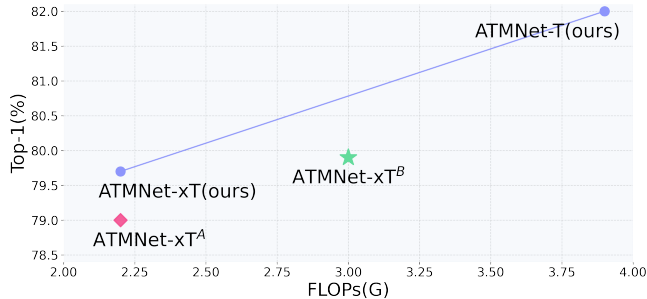


Figure 2: Comparisons of different offset configurations on ImageNet-1K. ATMNet-xT<sup>A</sup> (♦): offset learning is not decoupled along different directions, *i.e.*, the selected contextual tokens are directly recomposed as  $\tilde{\mathbf{x}} = [\mathbf{X}_{[i+oh_1, j+ow_1, 1]}, \mathbf{X}_{[i+oh_2, j+ow_2, 2]}, \dots]^T$  with the predicted offsets  $\{oh_c, ow_c\}$ . ATMNet-xT<sup>B</sup> (★): the number of selected contextual tokens per channel is extended from 1 to 3 for each direction.

## 4.5 Ablation Study and Analysis

**Effectiveness of ATM** Table 8 shows our ablation results. In the baseline ① of ATMNet, all offsets are fixed to 0, which means there is no spatial information interaction between different tokens in ①. This baseline achieves 79.3% accuracy on ImageNet-1K while its performance on dense prediction tasks is severely bounded due to the lack of adequate spatial interaction. This also validates that token mixing is sorely vital for dense prediction tasks. With our proposed ATMNet w/o PEG (②), the classification accuracy is improved by +2.7%, and the performance on the dense prediction task is *significantly improved by a large margin* (+7.4 mAP<sup>b</sup> on COCO and +7.7 mIoU on ADE20K). Our proposed ATM brings sufficient information mixing to help extract more powerful features with negligible additional computation overhead. The PEG module is introduced for providing position information for offset generation, which helps a little for dense tasks.

**Comparison with other offset configurations** 1) *Effectiveness of directional decomposition.* As show in Fig. 2, our ATMNet-xT is clearly superior to ATMNet-xT<sup>A</sup> (♦) with very close FLOPs, demonstrating the effectiveness of directional decomposition during predicting offsets. 2) *The number of selected contextual tokens.* The ATMNet-xT<sup>B</sup> (★) with more contextual tokens for each query outperforms ATMNet-xT by 0.2% but with +50% additional computa-

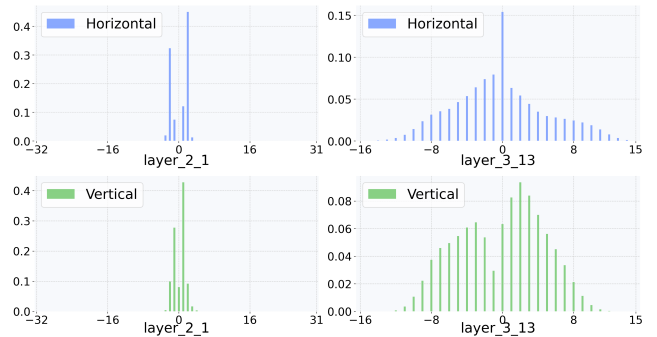


Figure 3: Histograms of learned offsets for the center token from different layers, counted on all samples from ADE20K val. The range of horizontal axis is the possible maximal range for the corresponding feature resolution, *e.g.*,  $[-32, 31]$  for the first sub-figure. Input size:  $512 \times 512$ . Feature resolutions for two columns:  $64 \times 64$  and  $32 \times 32$ . layer\_i\_j: j<sup>th</sup> layer of i<sup>th</sup> stage.

tion cost. This shows our ATM is a better trade-off between the computation cost and the final performance as an efficient and effective token mixer.

**Analyses of learned offsets** We investigate the distributions of the learned offsets via the histograms of offsets w.r.t. the center token in Fig. 3. We observe: 1) As the depth increases, the learned offsets expand to a larger range. This is in line with the conclusion in [46, 77] that local receptive fields in shallower layers are conducive to training vision models, while the long-range information is required for deeper layers. 2) For a query token, the learned offsets differ for different channels and such flexibility enables efficient semantic-adaptive information interaction. 3) Besides the network depth, the learned offsets of ATM are also adaptive to different datasets or tasks (shown in the Supplementary), endowing ATMNet with higher flexibility and better adaptivity. This observation indicates that mixing tokens with *hand-crafted and deterministic* rules is in fact insufficient to model the various distributions of different datasets. More results are in the Supplementary.

## 5 Conclusion

In this work, we propose an innovative token mixing mechanism, ATM, which actively and meticulously learns to fuse content-adaptive contextual information in the global scope. With the proposed basic operator, we build a general vision backbone ATMNet for various vision tasks and an enhanced FPN, *i.e.*, ATMFPN for dense prediction tasks. ATMNet is capable of flexibly and efficiently capturing diverse visual patterns. Comprehensive experiments demonstrate our ATMNet is generally applicable and effective for various vision tasks including image classification, object detection and semantic segmentation. In future work, we will exploit ATMNet’s potential of dealing with temporal video signals.



## References

- [1] A. Ali, H. Touvron, M. Caron, P. Bojanowski, M. Douze, A. Joulin, I. Laptev, N. Neverova, G. Synnaeve, J. Verbeek, et al. Xcit: Cross-covariance image transformers. *NeurIPS*, 34, 2021.
- [2] J. L. Ba, J. R. Kiros, and G. E. Hinton. Layer normalization. *arXiv preprint arXiv:1607.06450*, 2016.
- [3] D. Bau, J.-Y. Zhu, H. Strobelt, A. Lapedriza, B. Zhou, and A. Torralba. Understanding the role of individual units in a deep neural network. *Proceedings of the National Academy of Sciences*, 117(48):30071–30078, 2020.
- [4] G. Bertasius, H. Wang, and L. Torresani. Is space-time attention all you need for video understanding. *ICML*, 2(3):4, 2021.
- [5] Z. Cai and N. Vasconcelos. Cascade r-cnn: Delving into high quality object detection. In *CVPR*, pages 6154–6162, 2018.
- [6] N. Carion, F. Massa, G. Synnaeve, N. Usunier, A. Kirillov, and S. Zagoruyko. End-to-end object detection with transformers. In *ECCV*, pages 213–229. Springer, 2020.
- [7] K. C. Chan, X. Wang, K. Yu, C. Dong, and C. C. Loy. Understanding deformable alignment in video super-resolution. In *AAAI*, volume 35, pages 973–981, 2021.
- [8] S. Chen, E. Xie, C. GE, R. Chen, D. Liang, and P. Luo. CycleMLP: A MLP-like architecture for dense prediction. In *ICLR*, 2022.
- [9] X. Chen, B. Yan, J. Zhu, D. Wang, X. Yang, and H. Lu. Transformer tracking. In *CVPR*, pages 8126–8135, 2021.
- [10] B. Cheng, I. Misra, A. G. Schwing, A. Kirillov, and R. Girshick. Masked-attention mask transformer for universal image segmentation. *arXiv preprint arXiv:2112.01527*, 2021.
- [11] B. Cheng, A. Schwing, and A. Kirillov. Per-pixel classification is not all you need for semantic segmentation. In *NeurIPS*, volume 34, 2021.
- [12] F. Chollet. Xception: Deep learning with depthwise separable convolutions. In *CVPR*, pages 1251–1258, 2017.
- [13] X. Chu, Z. Tian, Y. Wang, B. Zhang, H. Ren, X. Wei, H. Xia, and C. Shen. Twins: Revisiting the design of spatial attention in vision transformers. *NeurIPS*, 34, 2021.
- [14] X. Chu, Z. Tian, B. Zhang, X. Wang, X. Wei, H. Xia, and C. Shen. Conditional positional encodings for vision transformers. *arXiv preprint arXiv:2102.10882*, 2021.
- [15] E. D. Cubuk, B. Zoph, J. Shlens, and Q. V. Le. Randaugment: Practical automated data augmentation with a reduced search space. In *CVPR Workshops*, pages 702–703, 2020.
- [16] J. Dai, H. Qi, Y. Xiong, Y. Li, G. Zhang, H. Hu, and Y. Wei. Deformable convolutional networks. In *ICCV*, pages 764–773, 2017.
- [17] J. Deng, W. Dong, R. Socher, L.-J. Li, K. Li, and L. Fei-Fei. Imagenet: A large-scale hierarchical image database. In *CVPR*, pages 248–255. Ieee, 2009.
- [18] X. Ding, X. Zhang, N. Ma, J. Han, G. Ding, and J. Sun. Repvgg: Making vgg-style convnets great again. In *CVPR*, pages 13733–13742, 2021.
- [19] X. Dong, J. Bao, D. Chen, W. Zhang, N. Yu, L. Yuan, D. Chen, and B. Guo. Cswin transformer: A general vision transformer backbone with cross-shaped windows. *arXiv preprint arXiv:2107.00652*, 2021.
- [20] K. He, X. Chen, S. Xie, Y. Li, P. Dollár, and R. Girshick. Masked autoencoders are scalable vision learners. *arXiv preprint arXiv:2111.06377*, 2021.
- [21] K. He, G. Gkioxari, P. Dollár, and R. Girshick. Mask r-cnn. In *ICCV*, pages 2961–2969, 2017.
- [22] K. He, X. Zhang, S. Ren, and J. Sun. Deep residual learning for image recognition. In *CVPR*, pages 770–778, 2016.
- [23] S. He, H. Luo, P. Wang, F. Wang, H. Li, and W. Jiang. Transreid: Transformer-based object re-identification. In *ICCV*, pages 15013–15022, 2021.
- [24] Q. Hou, Z. Jiang, L. Yuan, M.-M. Cheng, S. Yan, and J. Feng. Vision permutator: A permutable mlp-like architecture for visual recognition. 2021.
- [25] A. G. Howard, M. Zhu, B. Chen, D. Kalenichenko, W. Wang, T. Weyand, M. Andreetto, and H. Adam. Mobilenets: Efficient convolutional neural networks for mobile vision applications. *arXiv preprint arXiv:1704.04861*, 2017.
- [26] G. Huang, Z. Liu, L. Van Der Maaten, and K. Q. Weinberger. Densely connected convolutional networks. In *CVPR*, pages 4700–4708, 2017.
- [27] G. Huang, Y. Sun, Z. Liu, D. Sedra, and K. Q. Weinberger. Deep networks with stochastic depth. In *ECCV*, pages 646–661. Springer, 2016.
- [28] Y. Jiang, S. Chang, and Z. Wang. Transgan: Two pure transformers can make one strong gan, and that can scale up. *NeurIPS*, 34, 2021.
- [29] A. Kirillov, R. Girshick, K. He, and P. Dollár. Panoptic feature pyramid networks. In *CVPR*, pages 6399–6408, 2019.
- [30] A. Kolesnikov, A. Dosovitskiy, D. Weissenborn, G. Heigold, J. Uszkoreit, L. Beyer, M. Minderer, M. Dehghani, N. Houlsby, S. Gelly, T. Unterthiner, and X. Zhai. An image is worth 16x16 words: Transformers for image recognition at scale. In *ICLR*, 2021.
- [31] A. Krizhevsky, I. Sutskever, and G. E. Hinton. Imagenet classification with deep convolutional neural networks. *NeurIPS*, 25, 2012.
- [32] Y. LeCun, L. Bottou, Y. Bengio, and P. Haffner. Gradient-based learning applied to document recognition. *Proceedings of the IEEE*, 86(11):2278–2324, 1998.
- [33] K. Li, Y. Wang, P. Gao, G. Song, Y. Liu, H. Li, and Y. Qiao. Uniformer: Unified transformer for efficient spatiotemporal representation learning. *ICLR*, 2022.
- [34] Y. Li, C.-Y. Wu, H. Fan, K. Mangalam, B. Xiong, J. Malik, and C. Feichtenhofer. Improved multiscale vision transformers for classification and detection. *arXiv preprint arXiv:2112.01526*, 2021.
- [35] D. Lian, Z. Yu, X. Sun, and S. Gao. As-mlp: An axial shifted mlp architecture for vision. *ICLR*, 2022.
- [36] K. Lin, L. Wang, and Z. Liu. End-to-end human pose and mesh reconstruction with transformers. In *CVPR*, pages 1954–1963, 2021.
- [37] T.-Y. Lin, P. Dollár, R. Girshick, K. He, B. Hariharan, and S. Belongie. Feature pyramid networks for object detection. In *CVPR*, pages 2117–2125, 2017.
- [38] T.-Y. Lin, P. Dollár, R. Girshick, K. He, B. Hariharan, and S. Belongie. Feature pyramid networks for object detection. In *CVPR*, pages 2117–2125, 2017.
- [39] T.-Y. Lin, P. Goyal, R. Girshick, K. He, and P. Dollár. Focal loss for dense object detection. In *ICCV*, pages 2980–2988, 2017.
- [40] T.-Y. Lin, M. Maire, S. Belongie, J. Hays, P. Perona, D. Ramanan, P. Dollár, and C. L. Zitnick. Microsoft coco: Common objects in context. In *ECCV*, pages 740–755. Springer, 2014.

- [41] Z. Liu, H. Hu, Y. Lin, Z. Yao, Z. Xie, Y. Wei, J. Ning, Y. Cao, Z. Zhang, L. Dong, F. Wei, and B. Guo. Swin transformer v2: Scaling up capacity and resolution. In *CVPR*, 2022.
- [42] Z. Liu, Y. Lin, Y. Cao, H. Hu, Y. Wei, Z. Zhang, S. Lin, and B. Guo. Swin transformer: Hierarchical vision transformer using shifted windows. In *ICCV*, pages 10012–10022, 2021.
- [43] Z. Liu, H. Mao, C.-Y. Wu, C. Feichtenhofer, T. Darrell, and S. Xie. A convnet for the 2020s. *CVPR*, 2022.
- [44] I. Loshchilov and F. Hutter. Decoupled weight decay regularization. *ICLR*, 2019.
- [45] A. Paszke, S. Gross, F. Massa, A. Lerer, J. Bradbury, G. Chanan, T. Killeen, Z. Lin, N. Gimelshein, L. Antiga, A. Desmaison, A. Kopf, E. Yang, Z. DeVito, M. Raison, A. Tejani, S. Chilamkurthy, B. Steiner, L. Fang, J. Bai, and S. Chintala. Pytorch: An imperative style, high-performance deep learning library. In *NeurIPS*, pages 8024–8035. 2019.
- [46] M. Raghu, T. Unterthiner, S. Kornblith, C. Zhang, and A. Dosovitskiy. Do vision transformers see like convolutional neural networks? *NeurIPS*, 34, 2021.
- [47] M. Sandler, A. Howard, M. Zhu, A. Zhmoginov, and L.-C. Chen. Mobilenetv2: Inverted residuals and linear bottlenecks. In *CVPR*, pages 4510–4520, 2018.
- [48] K. Simonyan and A. Zisserman. Very deep convolutional networks for large-scale image recognition. *ICLR*, 2015.
- [49] C. Szegedy, S. Ioffe, V. Vanhoucke, and A. A. Alemi. Inception-v4, inception-resnet and the impact of residual connections on learning. In *AAAI*, 2017.
- [50] C. Szegedy, W. Liu, Y. Jia, P. Sermanet, S. Reed, D. Anguelov, D. Erhan, V. Vanhoucke, and A. Rabinovich. Going deeper with convolutions. In *CVPR*, pages 1–9, 2015.
- [51] C. Szegedy, V. Vanhoucke, S. Ioffe, J. Shlens, and Z. Wojna. Rethinking the inception architecture for computer vision. In *CVPR*, pages 2818–2826, 2016.
- [52] M. Tan, B. Chen, R. Pang, V. Vasudevan, M. Sandler, A. Howard, and Q. V. Le. Mnasnet: Platform-aware neural architecture search for mobile. In *CVPR*, pages 2820–2828, 2019.
- [53] M. Tan and Q. Le. Efficientnet: Rethinking model scaling for convolutional neural networks. In *ICML*, pages 6105–6114. PMLR, 2019.
- [54] C. Tang, Y. Zhao, G. Wang, C. Luo, W. Xie, and W. Zeng. Sparse mlp for image recognition: Is self-attention really necessary? *AAAI*, 2022.
- [55] Y. Tang, K. Han, J. Guo, C. Xu, Y. Li, C. Xu, and Y. Wang. An image patch is a wave: Phase-aware vision mlp. *arXiv preprint arXiv:2111.12294*, 2021.
- [56] I. O. Tolstikhin, N. Houlsby, A. Kolesnikov, L. Beyer, X. Zhai, T. Unterthiner, J. Yung, A. Steiner, D. Keysers, J. Uszkoreit, et al. Mlp-mixer: An all-mlp architecture for vision. *NeurIPS*, 34, 2021.
- [57] H. Touvron, P. Bojanowski, M. Caron, M. Cord, A. El-Nouby, E. Grave, G. Izacard, A. Joulin, G. Synnaeve, J. Verbeek, et al. Resmlp: Feedforward networks for image classification with data-efficient training. *arXiv preprint arXiv:2105.03404*, 2021.
- [58] H. Touvron, M. Cord, M. Douze, F. Massa, A. Sablayrolles, and H. Jégou. Training data-efficient image transformer distillation through attention. In *ICML*, volume 139, pages 10347–10357, July 2021.
- [59] H. Touvron, M. Cord, and H. Jégou. Deit iii: Revenge of the vit. *arXiv preprint arXiv:2204.07118*, 2022.
- [60] H. Touvron, M. Cord, A. Sablayrolles, G. Synnaeve, and H. Jégou. Going deeper with image transformers. In *ICCV*, pages 32–42, 2021.
- [61] G. Wang, Y. Zhao, C. Tang, C. Luo, and W. Zeng. When shift operation meets vision transformer: An extremely simple alternative to attention mechanism. *AAAI*, 2022.
- [62] J. Wang, K. Sun, T. Cheng, B. Jiang, C. Deng, Y. Zhao, D. Liu, Y. Mu, M. Tan, X. Wang, et al. Deep high-resolution representation learning for visual recognition. *TPAMI*, 43(10):3349–3364, 2020.
- [63] N. Wang, W. Zhou, J. Wang, and H. Li. Transformer meets tracker: Exploiting temporal context for robust visual tracking. In *CVPR*, pages 1571–1580, 2021.
- [64] W. Wang, E. Xie, X. Li, D.-P. Fan, K. Song, D. Liang, T. Lu, P. Luo, and L. Shao. Pyramid vision transformer: A versatile backbone for dense prediction without convolutions. In *ICCV*, pages 568–578, 2021.
- [65] W. Wang, E. Xie, X. Li, D.-P. Fan, K. Song, D. Liang, T. Lu, P. Luo, and L. Shao. Pvtv2: Improved baselines with pyramid vision transformer. *Computational Visual Media*, 8(3):1–10, 2022.
- [66] R. Wightman. Pytorch image models. <https://github.com/rwightman/pytorch-image-models>, 2019.
- [67] R. Wightman, H. Touvron, and H. Jégou. Resnet strikes back: An improved training procedure in timm. *arXiv preprint arXiv:2110.00476*, 2021.
- [68] Z. Wu, D. Lischinski, and E. Shechtman. Stylespace analysis: Disentangled controls for stylegan image generation. In *CVPR*, pages 12863–12872, 2021.
- [69] T. Xiao, Y. Liu, B. Zhou, Y. Jiang, and J. Sun. Unified perceptual parsing for scene understanding. In *ECCV*, pages 418–434, 2018.
- [70] E. Xie, W. Wang, Z. Yu, A. Anandkumar, J. M. Alvarez, and P. Luo. Segformer: Simple and efficient design for semantic segmentation with transformers. In *NeurIPS*, volume 34, 2021.
- [71] S. Xie, R. Girshick, P. Dollár, Z. Tu, and K. He. Aggregated residual transformations for deep neural networks. In *CVPR*, pages 1492–1500, 2017.
- [72] R. Xu, X. Xu, K. Chen, B. Zhou, and C. C. Loy. Stransgan: An empirical study on transformer in gans. *arXiv preprint arXiv:2110.13107*, 2021.
- [73] S. Yan, X. Xiong, A. Arnab, Z. Lu, M. Zhang, C. Sun, and C. Schmid. Multiview transformers for video recognition. *arXiv preprint arXiv:2201.04288*, 2022.
- [74] J. Yang, C. Li, P. Zhang, X. Dai, B. Xiao, L. Yuan, and J. Gao. Focal self-attention for local-global interactions in vision transformers. *NeurIPS*, 2021.
- [75] T. Yu, X. Li, Y. Cai, M. Sun, and P. Li. S2-mlp: Spatial-shift mlp architecture for vision. In *WACV*, pages 297–306, 2022.
- [76] S. Yun, D. Han, S. J. Oh, S. Chun, J. Choe, and Y. Yoo. Cutmix: Regularization strategy to train strong classifiers with localizable features. In *ICCV*, pages 6023–6032, 2019.
- [77] D. J. Zhang, K. Li, Y. Chen, Y. Wang, S. Chandra, Y. Qiao, L. Liu, and M. Z. Shou. Morphmlp: A self-attention free, mlp-like backbone for image and video. *arXiv preprint arXiv:2111.12527*, 2021.
- [78] H. Zhang, M. Cisse, Y. N. Dauphin, and D. Lopez-Paz. mixup: Beyond empirical risk minimization. *ICLR*, 2018.

- [79] H. Zhang, C. Wu, Z. Zhang, Y. Zhu, H. Lin, Z. Zhang, Y. Sun, T. He, J. Mueller, R. Manmatha, et al. Resnest: Split-attention networks. *arXiv preprint arXiv:2004.08955*, 2020.
- [80] S. Zheng, J. Lu, H. Zhao, X. Zhu, Z. Luo, Y. Wang, Y. Fu, J. Feng, T. Xiang, P. H. Torr, et al. Rethinking semantic segmentation from a sequence-to-sequence perspective with transformers. In *CVPR*, pages 6881–6890, 2021.
- [81] Z. Zhong, L. Zheng, G. Kang, S. Li, and Y. Yang. Random erasing data augmentation. In *AAAI*, volume 34, pages 13001–13008, 2020.
- [82] B. Zhou, H. Zhao, X. Puig, T. Xiao, S. Fidler, A. Barriuso, and A. Torralba. Semantic understanding of scenes through the ade20k dataset. *IJCV*, 127(3):302–321, 2019.
- [83] X. Zhu, H. Hu, S. Lin, and J. Dai. Deformable convnets v2: More deformable, better results. In *CVPR*, pages 9308–9316, 2019.
- [84] X. Zhu, W. Su, L. Lu, B. Li, X. Wang, and J. Dai. Deformable {detr}: Deformable transformers for end-to-end object detection. In *ICLR*, 2021.

## A1 More Architecture Details

Our ATMNet consists of four stages with downsampling layers inserted between every two stages. The downsampling layer is implemented by overlapping patch embedding [64, 65] with stride of 2, which reduces the spatial resolution in half. We illustrate the overall architecture of our ATMNet in Fig. 4 (a), and show the basic ATM block in Fig. 4 (b). Each ATM block consists of LayerNorm (LN) [2], ATM module, LN, and MLP sequentially with two skip connections. The MLP is composed of two Fully Connected (FC) layers which first increases the number of channels with a ratio  $E_i$  then reduces it to the original one. We find that it is not necessary to generate new offsets for each ATM block, instead we generate new offsets every  $K$  layers in each stage, where  $K = 2/2/6/6/6$  for the five variants ATMNet-xT/T/S/B/L, respectively. The detailed configurations of different architecture variants are listed in Table 10.

Config	Value
	xT, T, S, B, L
optimizer	AdamW
learning rate	1e-3
weight decay	0.05
batch size	1024
learning rate schedule	cosine decay
warmup epochs	5
training epochs	300
augmentation	RandAug (9, 0.5)
label smoothing [51]	0.1
mixup [78]	0.8
cutmix [76]	1.0
random erasing [81]	0.25
drop path [27]	0.1, 0.1, 0.2, 0.3, 0.3

Table 9: ImageNet-1K training settings.

We also present the distributions of the learned offsets on ImageNet-1K (image classification task) in Fig. 7. Besides the adaptivity to the network depth, we observe that the learned offsets of ATM are also adaptive to different datasets or tasks, endowing ATMNet with higher flexibility and better adaptivity. This observation also indicates that mixing tokens with hand-crafted and deterministic rules [8, 77, 24] is in fact insufficient to model the various distributions of different datasets.

## A2 More Experiment Results

### A2.1 Visualization of the Learned Offsets

We visualize the learned offsets in ATMNet for different input images in Fig. 5. There are two main observations: 1) The learned offsets are adaptive to the *scales* of visual contents. As illustrated in Fig. 5 (a) and (b), the token mixing is performed in a wider range for the query token located in large-scale object. 2) The learned offsets are adaptive to the *shapes* of visual contents. As illustrated in Fig. 5 (c) and (d), our ATMNet tends to mix tokens within semantic-relevant regions, exhibiting obvious shape adaptability.

### A2.2 Statistics of the Learned Offsets

We investigate the distributions of the learned offsets at different depths, and show the histograms of offsets w.r.t. the center token on COCO (object detection task) in Table 6. The histograms are counted over all samples from COCO val. As the depth increases, the learned horizontal/vertical offsets spread to larger receptive field. This is in line with the conclusion in [46, 77] that local receptive fields in shallower layers are conducive to training vision models, while the long-range information is required for deeper layers.



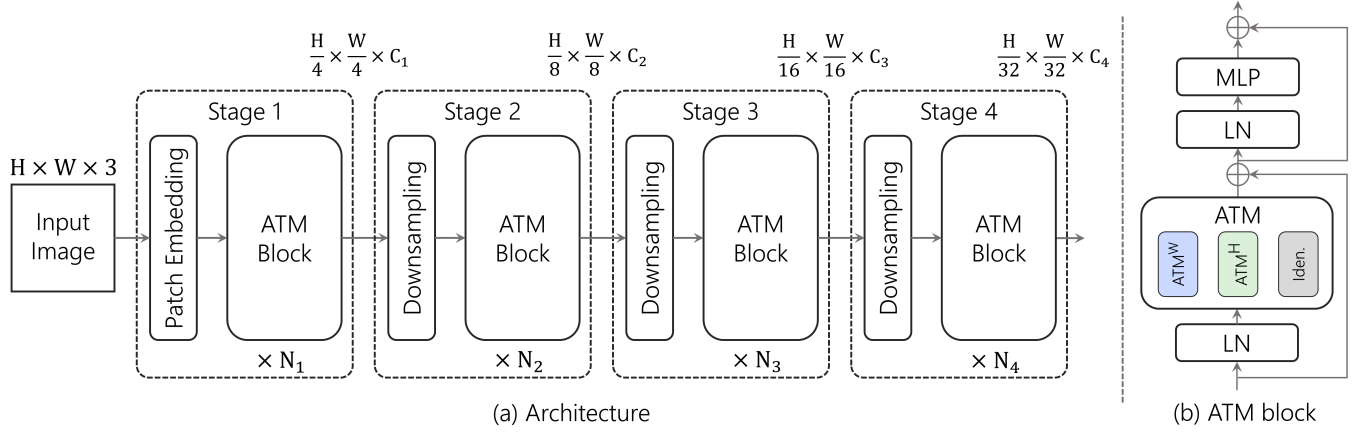


Figure 4: a) The overall architecture of ATMNet. b) The ATM block.

	Output size	Layer Name	-xT	-T	-S	-B	-L
Stage 1	$\frac{H}{4} \times \frac{W}{4}$	Overlapping Patch Embedding	$S_1 = 4$				
			$C_1 = 64$				
		ATM Block	$E_1 = 4$ $N_1 = 2$ $ \mathcal{O}_1  = 32$	$E_1 = 4$ $N_1 = 2$ $ \mathcal{O}_1  = 32$	$E_1 = 8$ $N_1 = 3$ $ \mathcal{O}_1  = 32$	$E_1 = 8$ $N_1 = 3$ $ \mathcal{O}_1  = 32$	$E_1 = 4$ $N_1 = 3$ $ \mathcal{O}_1  = 48$
Stage 2	$\frac{H}{8} \times \frac{W}{8}$	Downsampling	$S_2 = 2$				
			$C_2 = 128$				
		ATM Block	$E_2 = 4$ $N_2 = 2$ $ \mathcal{O}_2  = 32$	$E_2 = 4$ $N_2 = 3$ $ \mathcal{O}_2  = 32$	$E_2 = 8$ $N_2 = 4$ $ \mathcal{O}_2  = 32$	$E_2 = 8$ $N_2 = 8$ $ \mathcal{O}_2  = 32$	$E_2 = 4$ $N_2 = 4$ $ \mathcal{O}_2  = 48$
Stage 3	$\frac{H}{16} \times \frac{W}{16}$	Downsampling	$S_3 = 2$				
			$C_3 = 320$				
		ATM Block	$E_3 = 4$ $N_3 = 4$ $ \mathcal{O}_3  = 80$	$E_3 = 4$ $N_3 = 10$ $ \mathcal{O}_3  = 80$	$E_3 = 4$ $N_3 = 18$ $ \mathcal{O}_3  = 80$	$E_3 = 4$ $N_3 = 27$ $ \mathcal{O}_3  = 80$	$E_3 = 4$ $N_3 = 24$ $ \mathcal{O}_3  = 96$
Stage 4	$\frac{H}{32} \times \frac{W}{32}$	Downsampling	$S_4 = 2$				
			$C_4 = 512$				
		ATM Block	$E_4 = 4$ $N_4 = 2$ $ \mathcal{O}_4  = 64$	$E_4 = 4$ $N_4 = 3$ $ \mathcal{O}_4  = 64$	$E_4 = 8$ $N_4 = 4$ $ \mathcal{O}_4  = 64$	$E_4 = 8$ $N_4 = 8$ $ \mathcal{O}_4  = 64$	$E_4 = 4$ $N_4 = 4$ $ \mathcal{O}_4  = 96$

Table 10: Architecture variants.  $C_i$ ,  $E_i$ ,  $N_i$  and  $|\mathcal{O}_i|$  denote the number of channels, channel expand ratio, number of ATM blocks, and number of offsets per ATM block for the  $i^{th}$  stage.

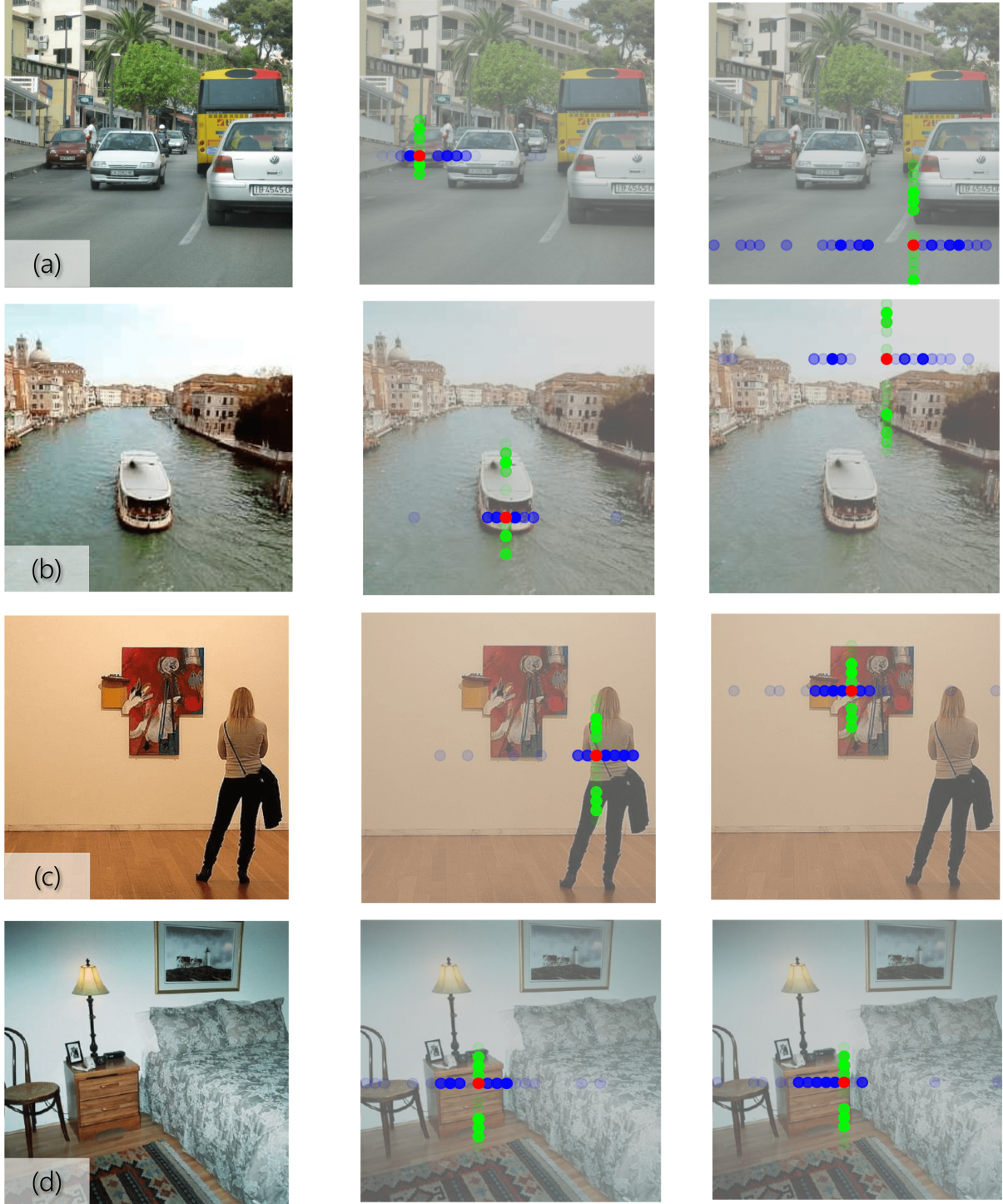


Figure 5: Illustration of the horizontal (●) and vertical (●) offsets for the given query token (●) on ADE20K (input size:  $512 \times 512$ ). The transparency of each circle corresponds to how many times the token at this position is sampled, i.e., the more transparent the circle is, the corresponding offset values appear less in  $\mathcal{O} = \{o_i\}_{i=1}^C$ . The visualized offsets are from a randomly sampled layer `layer_3_18`. Similar phenomena can be observed at other layers.

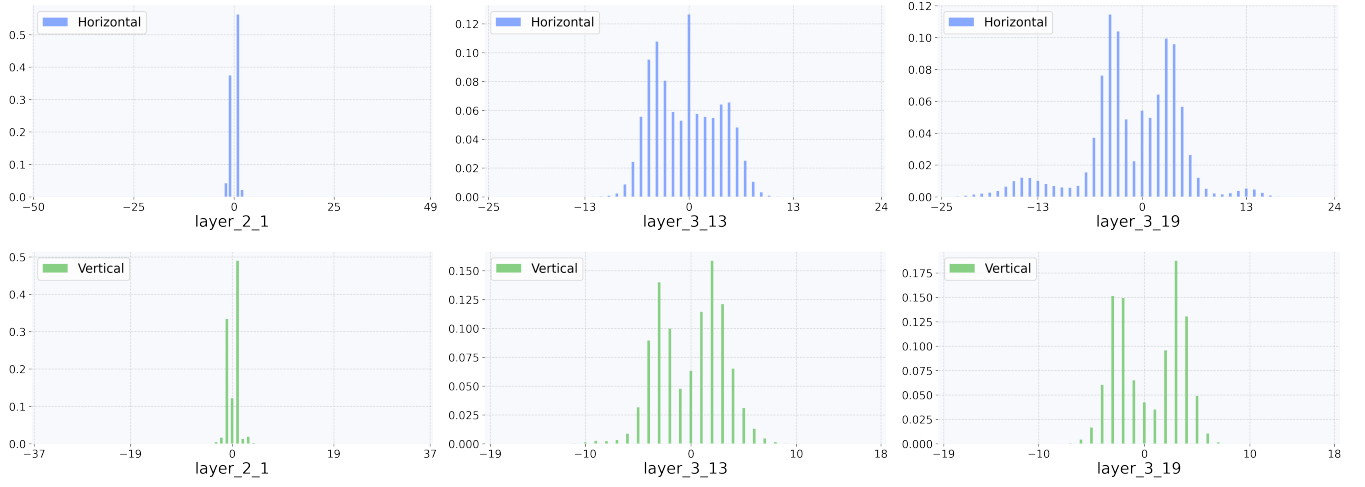


Figure 6: Histograms of learned offsets for the center token from different layers, counted on all samples from COCO val. The range of horizontal axis is the possible maximal range for the corresponding feature resolution, *e.g.*,  $[-50, 49]$  for the first sub-figure. Input size:  $600 \times 800$ . Feature resolutions for three columns:  $75 \times 100$ ,  $38 \times 50$  and  $38 \times 50$ . layer\_i-j:  $j^{th}$  layer of  $i^{th}$  stage.

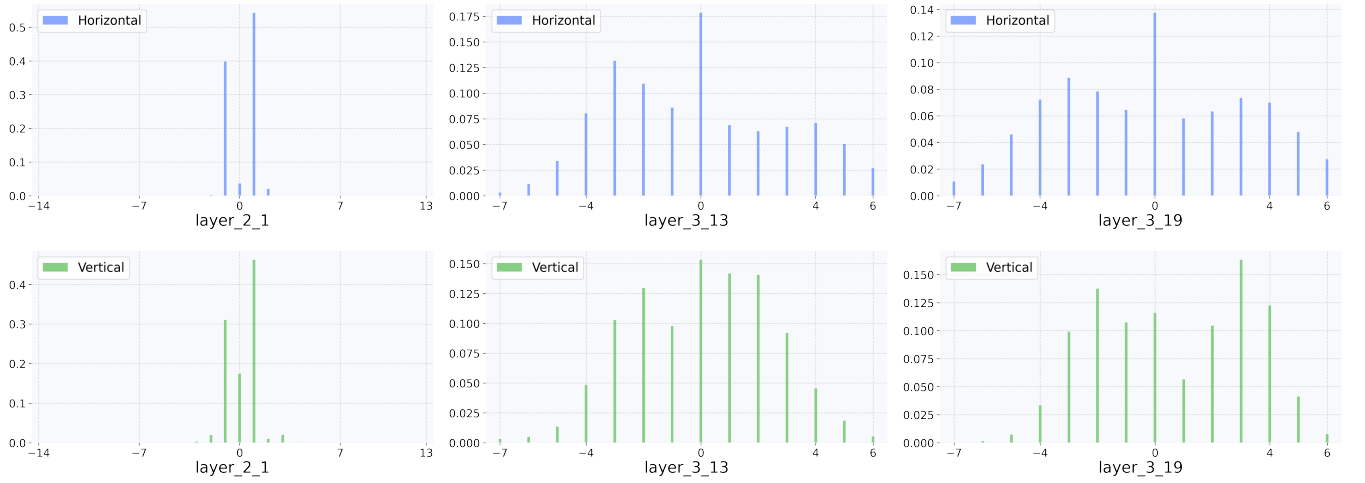


Figure 7: Histograms of learned offsets for the center token from different layers, counted on 5K random samples from ImageNet-1K val. The range of horizontal axis is the possible maximal range for the corresponding feature resolution, *e.g.*,  $[-14, 13]$  for the first sub-figure. Input size:  $224 \times 224$ . Feature resolutions for three columns:  $28 \times 28$ ,  $14 \times 14$  and  $14 \times 14$ . layer\_i-j:  $j^{th}$  layer of  $i^{th}$  stage.